Geochemistry, Geophysics, Geosystems

RESEARCH ARTICLE
10.1029/2019GC008538

Modeling the Inception of Supercontinent Breakup: Stress State and the Importance of Orogens

Chuan Huang[1,2], Nan Zhang[1,2], Zheng-Xiang Li[2], Min Ding[3], Zhuo Dang[1], Amaury Pourteau[2], and Shijie Zhong[4]

[1]Key Laboratory of Orogenic Belts and Crustal Evolution, School of Earth and Space Sciences, Peking University, Beijing, China, [2]Earth Dynamics Research Group, ARC Centre of Excellence for Core to Crust Fluid Systems and The Institute for Geoscience Research (TIGeR), Department of Applied Geology, Curtin University, Perth, Western Australia, Australia, [3]State Key Laboratory of Lunar and Planetary Sciences, Macau University of Science and Technology, Macau, China, [4]Department of Physics, University of Colorado, Boulder, CO, USA

Key Points:
- Plume push produces extensional stress of 20–50 MPa and plastic yielding in the inner region of a homogenous supercontinent with no orogen
- In supercontinent with weak orogens, the average tensile stress increases to ~160 MPa prior to plastic yielding (breakup) along orogens
- The presence of orogens promotes plate-like behavior during supercontinent breakup

Correspondence to:
N. Zhang,
nan_zhang@pku.edu.cn

Citation:
Huang, C., Zhang, N., Li, Z.-X., Ding, M., Dang, Z., Pourteau, A., & Zhong, S. (2019). Modeling the inception of supercontinent breakup: Stress state and the importance of orogens. *Geochemistry, Geophysics, Geosystems*, *20*. https://doi.org/10.1029/2019GC008538

Received 1 JUL 2019
Accepted 12 SEP 2019
Accepted article online 15 OCT 2019

Abstract The relative significance of various geodynamic mechanisms that drive supercontinent breakup is unclear. A previous analysis of extensional stress during supercontinent breakup demonstrated the importance of the plume-push force relative to the dragging force of subduction retreat. Here, we extend the analysis to basal traction (shear stress) and cross-lithosphere integrations of both extensional and shear stresses, aiming to understand more clearly the relevant importance of these mechanisms in supercontinent breakup. More importantly, we evaluate the effect of preexisting orogens (mobile belts) in the lithosphere on supercontinent breakup process. Our analysis suggests that a homogeneous supercontinent has extensional stress of 20–50 MPa in its interior (<40° from the central point). When orogens are introduced, the extensional stress in the continents focuses on the top 80-km of the lithosphere with an average magnitude of ~160 MPa, whereas at the margin of the supercontinent the extensional stress is 5–50 MPa. In both homogeneous and orogeny-embedded cases, the subsupercontinent mantle upwellings act as the controlling factor on the normal stress field in the supercontinent interior. Compared with the extensional stress, shear stress at the bottom of the supercontinent is 1–2 order of magnitude smaller (0–5 MPa). In our two end-member models, the breakup of a supercontinent with orogens can be achieved after the first extensional stress surge, whereas for a hypothetical supercontinent without orogens it starts with more diffused local thinning of the continental lithospheric before the breakup, suggesting that weak orogens play a critical role in the dispersal of supercontinents.

1. Introduction

Supercontinent breakup is a key step of supercontinent cycles and therefore an important aspect of Earth's dynamic evolution (Bleeker, 2003; Bradley, 2011; Collins, 2003; Li et al., 2008; Rogers & Santosh, 2003; Yoshida & Santosh, 2011). The current configuration of the major continents on Earth's surface is a direct result of the breakup of the supercontinent Pangea (Seton et al., 2012). Understanding what drives the breakup of supercontinents is crucial for understanding the dynamic driving force of plate tectonics. Major forces being considered include the push force from uprising subcontinental mantle plumes (Buiter & Torsvik, 2014; Cande & Stegman, 2011; Gurnis, 1988; Koptev et al., 2015; Li et al., 1999, 2008; Zhang et al., 2018), the traction force of mantle convection (Morgan, 1972; Wilson, 1973), and the drag force from retreating subduction at the margin of the supercontinent (e.g., Bercovici & Long, 2014; Dal Zilio et al., 2018; Lowman & Jarvis, 1995; Yoshida, 2017). Among the three mechanisms, it has been argued that the extensional force caused by plume push is more important than that from subduction retreat at least during the early stage of the breakup (Zhang et al., 2018). The plume-push force appears to dominate the extensional stress at the shallow depths of the continental lithosphere at the interior of the supercontinent, whereas extension caused by subduction retreat mainly focuses along the marginal zone of the supercontinent (Zhang et al., 2018). However, the contribution of convection-induced basal traction to the breakup (e.g., Yoshida, 2019) has not been fully investigated. Also, previous studies of full stress distribution in the continental lithosphere during supercontinent breakup were mainly limited to two-dimensional (2-D) models (e.g., Ulvrova et al., 2019). More importantly, the effects of preexisting orogens (or mobile belts, e.g., Nyblade & Robinson, 1994) in the supercontinent on stress distribution and the

timing of breakup have not been thoroughly addressed (Yoshida, 2013; Yoshida, 2014; Rolf et al., 2014; Ulvrova et al., 2019).

Many previous studies of supercontinent dynamics explored the roles of self-consistently generated mantle plumes under a supercontinent (Gurnis, 1988; Lowman & Jarvis, 1995; Zhong & Gurnis, 1995; Phillips & Bunge, 2007; Zhong et al., 2007; Li & Zhong, 2009; Zhang et al., 2009; Rolf et al., 2012; Yoshida & Santosh, 2014; Zhang et al., 2018). These studies commonly emphasized the importance of plume-push force during the breakup of the supercontinent. Works focusing on the stress produced by subduction retreat (Bercovici & Long, 2014; Dal Zilio et al., 2018; Holt et al., 2015; Lowman & Jarvis, 1995; Lu et al., 2015; Yoshida, 2017), on the other hand, either omitted the plume-push force and the interaction between plumes and subduction retreat (e.g., Dal Zilio et al., 2018), or inserted ad-hoc plumes beneath the continent (e.g., Lu et al., 2015). The capacities of these latter studies in exploring the full force of supercontinent breakup are therefore restricted by their inability of generating dynamically self-consistent plumes (or plume cluster) beneath the supercontinent.

In this study, we extend our 3-D analysis (Zhang et al., 2018) to basal traction (shear stress) and integrals of stresses by using supercontinent dynamic modeling in which a subduction girdle and corresponding return plumes (plume cluster) are self-consistently generated, so to understand the full stress field and total force that drive supercontinent breakup. These stresses and integrated total force are quantified and compared to determine the contributions of different mechanisms to the breakup of supercontinents. In addition, we evaluate the significance of preexisting orogens in supercontinent breakup. Orogens typically have thinner lithosphere compared to cratons, and are mechanically weaker (Hyndman et al., 2005). Their impacts on the breakup of supercontinents have previously been noted (e.g., Buiter & Torsvik, 2014; Storey, 1995). For example, the opening of the Atlantic Ocean followed the Caledonian orogen, the Appalachian orogen, and the West Congo-Aracuai Belt (Dietz & Holden, 1970; Holbrook et al., 1994; Tupinambá et al., 2007; Torsvik et al., 2009; Heine et al., 2013). Although orogens are known to cause strain localization (Lenardic et al., 2003; Yoshida, 2013), none of the previous models has quantitatively explored the orogen-induced stress variation during the breakup of supercontinents. Hence, this study aims to investigate the roles of plastic yielding in a homogeneous supercontinent and strain concentration along preexisting orogens as failure mechanisms for the breakup of supercontinents. We also explore the different evolution processes of continental dispersal in two groups of models, although similar modelings were previously attempted in 2-D settings (Gurnis, 1988; Lowman & Jarvis, 1995).

The paper is arranged as follows: section 2 describes the governing equations, the key parameters, the definition of supercontinent breakup time, the setting of weak orogens in supercontinents, and the method for stress analysis. Section 3 shows the results of normal and shear stresses as well as their integrals, and the general stress state evolution after the breakup. Section 4 mainly discusses the dispersion of continental blocks after supercontinent breakup in 3-D spherical domain as well as the limitations of our modeling results. This is followed by section 5, conclusions.

2. Numerical Model Setup

2.1. Governing Equations

We build the dynamic models of mantle convection with continental blocks in a three-dimensional spherical geometry with infinite Prandtl number and the Boussinesq approximation. The nondimensional governing equations for thermo-chemical mantle convection are (e.g., Zhong et al., 2008; McNamara & Zhong, 2004):

$$\nabla\cdot\mathbf{u} = 0, \tag{1}$$

$$-\nabla p + \nabla\cdot\left[\eta\left(\nabla\mathbf{u} + \nabla\mathbf{u}^T\right)\right] - \left(RaT - \sum_{i=1}^{2} Ra_{c\_i}C_i\right)\mathbf{g} = 0, \tag{2}$$

$$\frac{\partial T}{\partial t} + \mathbf{u}\cdot\nabla T = \nabla^2 T + H, \tag{3}$$

$$\frac{\partial C_i}{\partial t} + \mathbf{u}\cdot\nabla C_i = 0. \tag{4}$$

Table 1
Physical Parameters and Their Values

Parameter	Value[a]
Earth radius R	6,371 km
Mantle thickness d	2,870 km
Thermal expansivity α	3×10^{-5}/K
Thermal diffusivity κ	1×10^{-6} m^2/s
Surface density ρ	3,400 kg/m^3
Surface specific heat C_p	1,200 J $\cdot$ kg^{-1} $\cdot$ K^{-1}
Surface gravitational acceleration g	10.0 m/s^2
Activation energy E	100 kJ/mol
Reference Temperature T_r	1,600 K
Temperature offset T_o	900 K
Internal heating H	80 (7.38×10^{-12} W/kg) [0 for Case 2]
Surface temperature T_s	273 K
Reference Viscosity η_{ref}	1×10^{22} Pa s [3×10^{21} Pa s for Case 3; 3×10^{22} Pa s for Case 4]
Temperature contrast between surface and CMB ΔT	3,000 K

[a]For a nondimentional parameter (note we use Earth's radius to scale the length in a unit), the true value is shown in the parentheses. If the parameter has multiple settings, all possible values are given in the brackets.

Here the variables are the velocity vector $\mathbf{u}$, dynamic pressure p, viscosity η, temperature T, chemical composition C_i ($0\leq C_i\leq 1$, 0 for the mantle, 1 for the chemical (cratons if $C_1 = 1$, orogens if $C_2 = 1$) materials), time t, and internal heat generation rate H. Ra and Ra_{c_i} are the Rayleigh number and chemical Rayleigh numbers, respectively. They are defined as

$$Ra = \frac{\alpha\rho g\Delta T R^3}{\kappa\eta_{\text{ref}}}, \tag{5}$$

$$Ra_{c\_i} = Ra\frac{\Delta\rho_{c\_i}}{\rho\alpha\Delta T}, \tag{6}$$

where α, ρ, g, ΔT, R, κ, η_{ref}, and $\Delta\rho_{c\_i}$ are the thermal expansivity, density, gravitational acceleration, temperature difference between the core-mantle boundary (CMB) and the surface, radius of the Earth, thermal diffusivity, reference viscosity, and density contrast between continents (including orogens) and the surroundings, respectively (Table 1). Note the definition of Rayleigh number is based on Earth's radius rather than the thickness of the mantle, with that based on the former being ~10 times of that based on the latter.

The viscosity used in our model depends on the depth, temperature, and composition as:

$$\eta = \eta_r(r)\prod_{i=0}^{2}\eta_c(C_i)^{f_i}\exp\left(\frac{E}{T+T_o}-\frac{E}{T_r+T_o}\right). \tag{7}$$

Here $\eta_r(r)$ is the depth-dependent viscosity prefactor, $\eta_c(C_i)$ is the viscosity jump for chemically distinct materials (100 for cratrons, 1 for orogens), f_i is the fraction of the ith composition in an element, E is the activation energy, and T_r and T_o are the reference temperature and temperature offset, respectively (Table 1). We choose $\eta_r(r)$=1/30 for the upper mantle except for the mantle lithosphere (depth < 150 km) where $\eta_r(r)$=1 (Zhong et al., 2007). For the lower mantle, $\eta_r(r)$ increases linearly from $\eta_r(r) = 1$ at the 660-km depth to $\eta_r(r) = 3$ at the CMB (Zhang, Zhong, et al., 2010). The term $\prod_{i=0}^{2}\eta_c(C_i)^{f_i}$ in equation (7) manifests that the composition-related viscosity in an element is calculated by the geometric average of all the chemical parts in it. The corresponding dimensional activation energy E is 100 kJ/mol in both the upper (Flament et al., 2014) and lower mantle, giving a ~10^3 times viscosity drop in the convective mantle when T changes from 0 to 1. This temperature-induced viscosity change is smaller than that in some other studies (e.g., Rolf & Tackley, 2011). However, the viscosity decrease in the upper mantle (>150-km depth) due to depth-related multiplier $\eta_r(r)$ ensures the generation of a relatively high viscous lithosphere (Figure 1b).

Besides equation (7), yielding in the continental lithosphere is considered in the model as the failure mechanism when convective stress exceeds the yield stress. It follows the form of

$$\eta_y = \frac{\sigma_y}{2\dot{\varepsilon}_{II}}, \tag{8}$$

where η_y, σ_y, and $\dot{\varepsilon}_{II}$ are the nondimensional yielding viscosity, yield stress, and second invariant of strain-rate tensor, respectively. The final effective viscosity η_e is a combination of equations (7) and (8), given by

$$\eta_e = \left(\frac{1}{\eta}+\frac{1}{\eta_y}\right)^{-1}. \tag{9}$$

This plasticity formulation is widely used in mantle convection simulations (e.g., Foley & Becker, 2009; Rolf et al., 2012; Tackley, 2000; Yoshida, 2014).

The reference Rayleigh number used in our model is ~8×10^7 with corresponding reference viscosity of 10^{22} Pa $\cdot$ s beneath the 660-km depth. The resulting viscosity profile in our model (Figure 1b) is comparable with the results of geophysics inversions (e.g., Mitrovica & Forte, 2004). The nondimensional internal heat generation rate of H is set to 80 (or ~7.38×10^{-12} W/kg) based on the estimation of Turcotte and Schubert

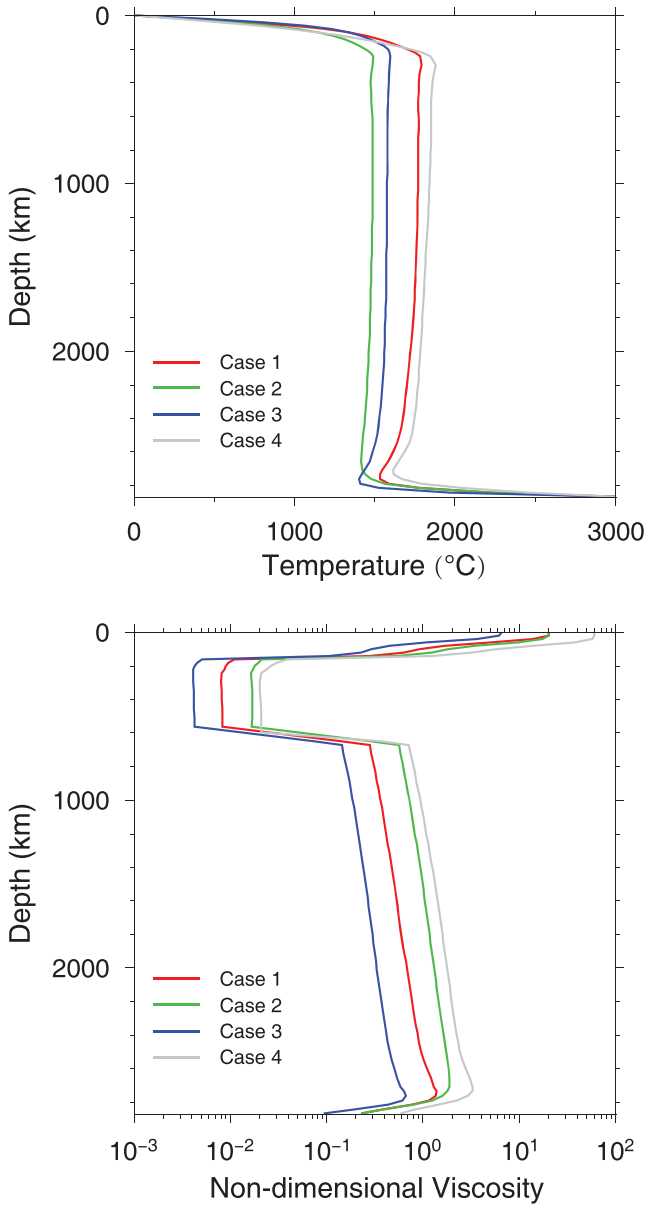

Figure 1. The initial (a) temperature and (b) nondimentional viscosity profiles for Case 1 (red line), Case 2 (green line), Case 3 (blue line) and Case 4 (gray line).

(2014). The nondimensional radii for the top and bottom boundaries are 1 and 0.55, respectively. Free-slip and isothermal boundary conditions are applied at the surface and the CMB in all calculations. Our convection models are computed using code CitcomS (Zhong et al., 2008) in which the tracer ratio method (McNamara & Zhong, 2004; Tackley & King, 2003) with ~8×10^7 tracers is used to solve the transport of chemical components. The mantle is divided into 12 caps and each cap contains 64×64×64 elements. The elements in the lithosphere are further refined in the radial direction with a resolution of 20 km per element. The numerical resolution this work is an improvement over that of Zhang et al. (2009, 2018).

2.2. Key Model Parameters

Similar to Zhong et al. (2007) and Zhang et al. (2009), supercontinent in this work is simplified as a 200-km thick (e.g., Gung et al., 2003) spherical disc. The disc occupies 30% (e.g. Zhong et al., 2007) of the Earth's surface with corresponding great circle arc of 66.4° from the disc center to its edge. The model supercontinent is defined as a chemically distinct material by assigning the composition-related viscosity factor η_c and extra density $\Delta\rho_c$. Here η_c is set to be 100 times of the viscosity of oceanic lithosphere (Yoshida, 2014; Zhang et al., 2009). The $\Delta\rho_c$ is set to be -50 kg/m^3 (Poudjom Djomani et al., 2001; Rolf et al., 2012; Yoshida, 2013).

We also apply a 200-km-wide weak zone at the supercontinent's boundary to allow the surrounding oceanic lithosphere to subduct (e.g., Zhong et al., 2007). The depth of the weak zone is 150 km, same as the thickness of the oceanic lithosphere. Since we do not take the weak zone as of chemically distinct materials from the oceanic lithosphere, it is tracked by the distance away from the center of the supercontinent. For example, the typical retreating rate of the subduction zone is 1–2 cm/yr following Schellart et al. (2008). To define the position of a trench, we firstly recompute the position of the weak zone based on a given rate of subduction retreat, and then reassign a new viscosity here at every time step. In this work, the viscosity of the weak zone is either 1/30 or 1/100 of that of the oceanic lithosphere, consistent with the range of 0.01–0.1 used by previous studies (e.g., Holt et al., 2015; Yoshida, 2017; Zhong et al., 2007). For supercontinent with orogens, the weak zone is segmented where orogens meet the edge of the supercontinent (Figure 2).

The depth-averaged differential stress (or strength) in the continental interior based on laboratory experiments is <300 MPa (figure 9 of Kohlstedt et al., 1995). Also, from load-induced surface deformation in Hawaii (Zhong & Watts, 2013), the estimated maximum stress in the deformed lithosphere is 100–200 MPa. The two studies provide the most straightforward estimations of the lithospheric strength. In this work, we choose the 100 MPa as the default yield strength of the continental lithosphere. The value is consistent with previous dynamic works (e.g., Yoshida, 2010; Mallard et al., 2016).

2.3. Initial Conditions and Defining the Supercontinent Breakup Time

Our model has an initial temperature profile obtained from the statistical steady-state thermal field of a precalculation (Figure 1a). At the beginning of the model, the supercontinent disc and a surrounding weak zone are introduced. The latter promotes the formation of circum-supercontinent subduction, that is, the subduction girdle. As the subduction slabs enter the lower mantle, hot structures beneath the supercontinent initiate (Figure 3c; e.g., Zhong et al., 2007). These hot structures are self-consistently generated by the subduction girdle. Most of the upwelling structures concentrate beneath the central region (<35°from the center) of the

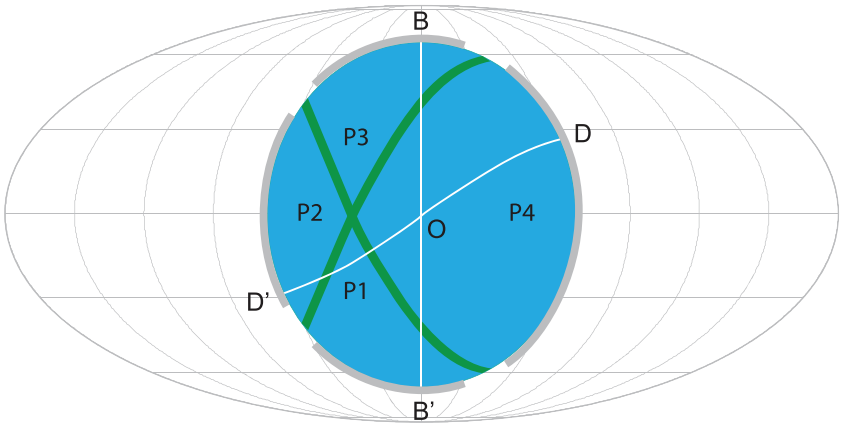

Figure 2. (a) A sketch showing the positions of two intersecting orogens (thick green lines) in a supercontinent (blue area). The two orogens divide the supercontinent into four parts (denoted as "P1," "P2," "P3," and "P4"). The supercontinent is centered at longitude=0° and latitude=0°. $\dot{B}OB'$ and $\dot{D}OD'$ (white lines) are traverses along great circles crossing the supercontinent's center *O*. The four gray belts near the supercontinent's margin represent four separated subduction zones.

supercontinent. The configuration of the subsupercontinent plumes in our model is similar to that in 2-D modelings (e.g., Heron et al., 2015).

To analyze the relationship between changes in mantle thermal state and supercontinent breakup (Rolf et al., 2014; Yoshida, 2013), we examine the evolution of subsupercontinent average temperature from the bottom of the supercontinent to the CMB (red curve in Figure 3a) and more importantly, the average temperature in region right below the continental lithosphere (200- to 300-km depth; green curve in Figure 3 a). We find that the average temperature of the whole subsupercontinent mantle starts to increase quickly after about one transit time, *t*0 (i.e., one transit time is the time it takes for a particle to travel from the surface to the CMB with the average surface horizontal velocity, or ~60 Ma in this study) with the first arrival of cold slabs on the CMB (Figure 3c), similar to that in Zhong et al. (2007).

After one more transit time at time *t1* (Figure 3a), subcontinental plume heads (or plume cluster) reach the bottom of the continental lithosphere (Figure 3d), initiating the lithospheric erosion at the bottom of the supercontinent (see the zoom-in in Figure 3e). At this time (*t*1 at 123 Myr), several important physical variables reach their maxima: the erosion at the bottom of the continental lithosphere is the most vigorous; the average subsupercontinent (200–300 km in depth) temperature becomes the highest (green line in Figure 3a); and the average extensional stress in the shallow depth (0–40 km) for the homogenous supercontinent (or the average extensional stress in the orogenic intersection for orogen-embedded supercontinent; see section 3.1.2) reaches its maximum as shown by the black curve (blue curve for the orogen-embedded supercontinent) in Figure 3b. Previous studies (Gurnis, 1988; Lowman & Jarvis, 1995) also used the maximum stress as the time indicator for a supercontinent breakup. After the time point *t*1, the stress drops rapidly, which we take as an indication of lithospheric failure and thus the beginning of supercontinent breakup. The time period between *t*0 and *t*1 in our model roughly coincides with the time between the observed emergence of LIP occurrences (e.g., Pangean LIPs commonly appeared 50 Ma after its formation; Neumann et al., 1992; Kamo et al., 1996; Courtillot et al., 1999; Veevers, 2004; Li & Zhong, 2009; Zhang, Li, et al., 2010) and the first appearance of oceanic crust during the breaking-up of Pangea (~150 Myr after Pangea formation).

From the breakup time *t1*, we start to examine the effects of plastic yielding of the supercontinent and the retreat of the subduction girdle. We do the stress analysis with the model stress tensor fields (Zhong et al., 2008). Although we focus on the stress state right after *t*1 (<1 Myr) in section 3, we also track the stress evolution for 50 Myr after *t*1 in section 4.2.

2.4. Orogens in Supercontinent

In our model with arbitrary orogens (mobile belts), we prescribe two intersecting orogens in the supercontinent. Each orogen is modeled as a 400-km-wide (e.g., Rivers, 2015) arc along a great circle (thick green lines in Figure 2) with same thickness (and density) of the continental lithosphere (200 km), but much lower

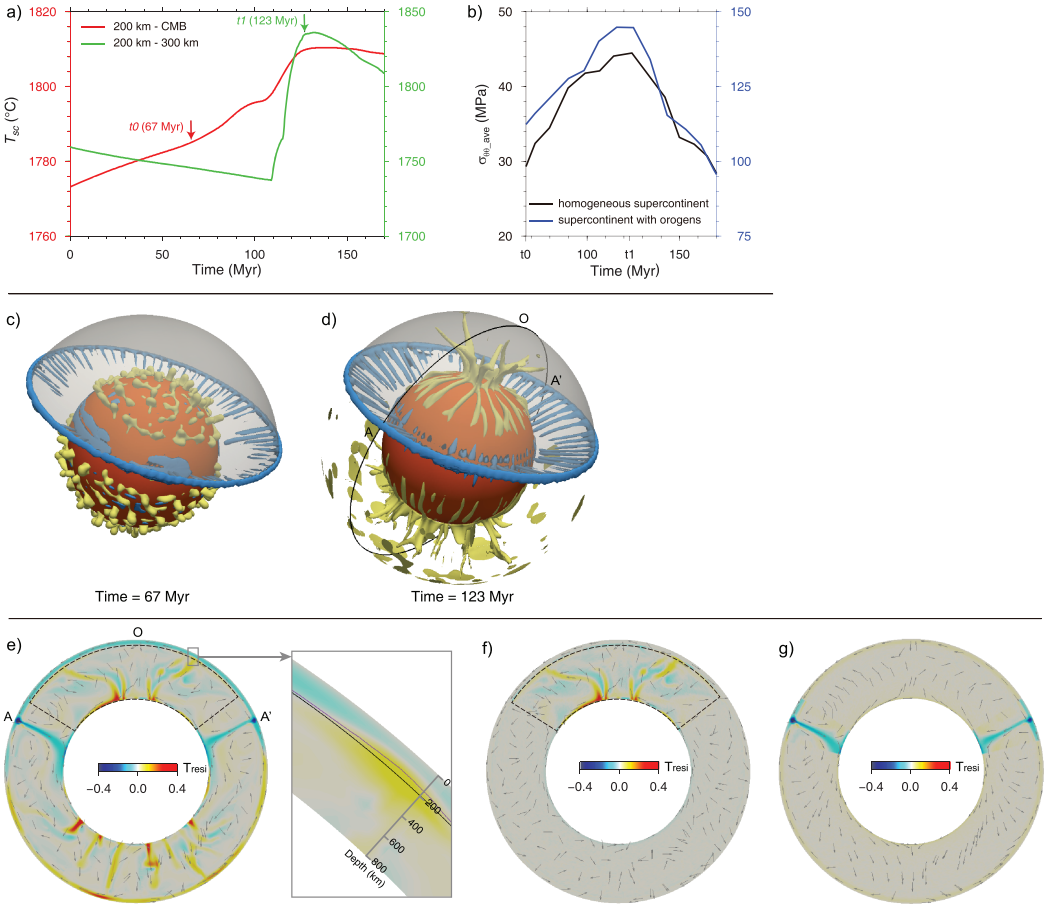

Figure 3. (a) Case 1 with red and green lines showing the time-dependent (from the beginning of model to ~170 Myr after it) subsupercontinent mantle (from the supercontinent bottom to the CMB) mean temperature and the average temperature within 100 km right beneath (200–300 km in depth) the supercontinent, respectively. (b) Black and blue curves showing the stress variations after *t*0 (67 Myr) for Cases 1i and 1j, respectively. The stresses are averaged at 0–40 km depth in either the inner 40° of the supercontinent (Case 1i) or the region that two orogens intersect (Case 1j). (c) and (d) Thermal structures for Case 1 at *t*0 and *t*1 (123 Myr in (a)), respectively. The thermal structures are plotted as contours of residual nondimentional temperature with values respectively at 0.1 (yellow for hot mantle) and −0.1 (blue for cold mantle). The semitransparent gray caps in (c) and (d) show the position of supercontinent. (e) Nondimensional residual temperature and velocity fields on cross section $\overset{\frown}{AOA'}$ in (d). The black and purple lines in the zoom-in of the rectangle box represent the bottom of the continental lithosphere at 67 Myr (*t*0) and 123 Myr (*t*1), respectively. (f) and (g) give the resolved hot structures beneath the supercontinent (region surrounded by black dashed line in (e) and (f)) and cold structures at the periphery of subduction zone, respectively.

viscosity (thus significantly weaker). These two great circle arcs do not pass through the center of the supercontinent but intersect at a point at 30° away from the supercontinent center, with each great circle arc defining a plane 60° away from the equatorial plane. The orogens consist of chemically distinct materials ($C_2 = 1$) with the same viscosity as the oceanic lithosphere. The topography of the orogens is not considered due to the limitation of the free-slip boundary condition. The influence of topography on stress state will be discussed in section 4.3.

2.5. Analysis on Stresses and Integrated Forces

The velocity field of the homogeneous supercontinent at breakup time shows a divergent pattern from supercontinent center to the edge (section 4.1; Zhang et al., 2018), which inspires us to focus on the normal and shear stresses along this direction. To achieve a representative stress state, we calculate the average stresses in 12 evenly spaced lithospheric transects crossing the supercontinent center (e.g., $\overset{\frown}{OA}$ in Figure 4, where *O* is the supercontinent center). For element *E* in the transects (Figure 4), local normal stress and shear stress are

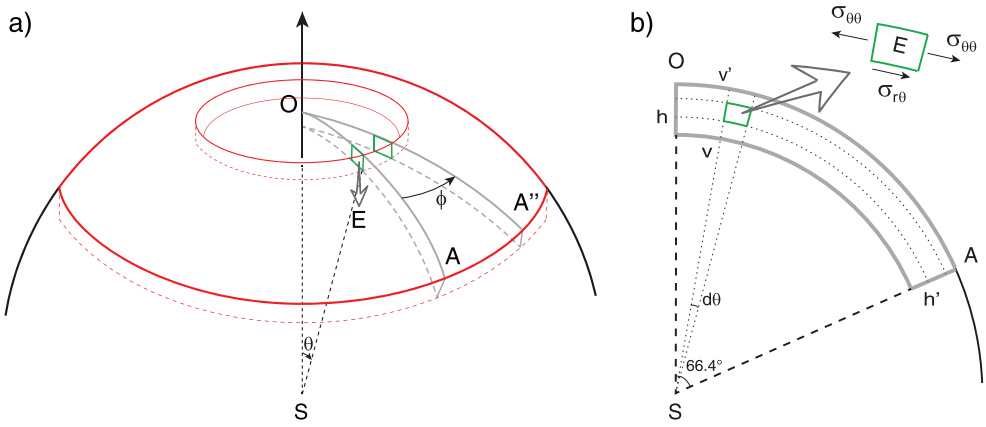

Figure 4. (a) A sketch showing an arbitrary element E (green box) in the supercontinent (region surrounded by thick red line) in a 3-D view. A more clear presentation of normal and shear stresses for this element on 2-D cross section OA in (a) is given in (b). Dashed lines hh' and vv' in (b) show the integrating ranges for integrals F_h and F_v, respectively.

obtained by Cauchy stress transformation (Reddy, 2013; also see Figure 3 and equation (10) in Zhang et al., 2018). We will show the distribution of the normal stress $\sigma_{\theta\theta}$ in the whole lithospheric transect and shear stress $\sigma_{r\theta}$ at the bottom of the supercontinental in section 3.

The integral forces of $\sigma_{\theta\theta}$ along the vertical axis (i.e., integral of along vv' in Figure 4b) and $\sigma_{r\theta}$ along the azimuth direction (i.e., integral of $\sigma_{r\theta}$ along hh' in Figure 4b) are calculated through equations

$$F_v = \int_{r=Sv}^{r=Sv+200\,\mathrm{km}} \sigma_{\theta\theta} dr \tag{10}$$

and

$$F_h = \int_{\theta=0}^{\theta=66.4} \sigma_{r\theta} r(\pi/180) d\theta, \tag{11}$$

respectively, where F_v and F_h are functions of r and θ, respectively. Both F_v and F_h represent horizontal forces acting on the supercontinent. These two integrals provide assessments for the extensional force and basal traction per unit length in direction ϕ (Figure 4a). The "force" used here is similar to the ridge push force from Turcotte and Schubert (2014).

For the supercontinent with orogens, the divergent center of the supercontinent coincides with the intersection of the orogens (see section 4.1 for discussion). Therefore, instead of the average stress on the 12 evenly spaced slices, stress state along two manually selected arcs ($\hat{BOB'}$ and $\hat{DOD'}$ in Figure 2) is computed. For the same reason, stress integral in azimuth direction, that is, F_h, is ignored.

3. Results

We present our calculated stresses in a supercontinent in two groups of models: with and without orogens. We focus on the stress distribution and integrated forces at the time of supercontinent breakup.

3.1. Stresses and Forces in A Homogenous Supercontinent without Orogens

3.1.1. The Average Stresses in 2-D Cross Sections

We first present the stress state of the reference case (Case 1) in which the yield stress, the relative viscosity of the subduction weak zone, and the rate of subduction retreat are set at 100 MPa, 1/30 and 2 cm/year, respectively. As shown in Figure 5a, the extensional stress in supercontinent interior (from supercontinent's center to 40° away), especially the topmost 80 km of the lithosphere, is positive (20–50 MPa). The stress concentration in the upper part (<80 km) of the continental lithosphere reflects the higher viscosity there than the lower part. In regions closer to the supercontinent edge, the normal stress changes to negative, while subduction retreat causes the stress in the marginal weak zone to be extensional (Figure 5a). This stress variation is

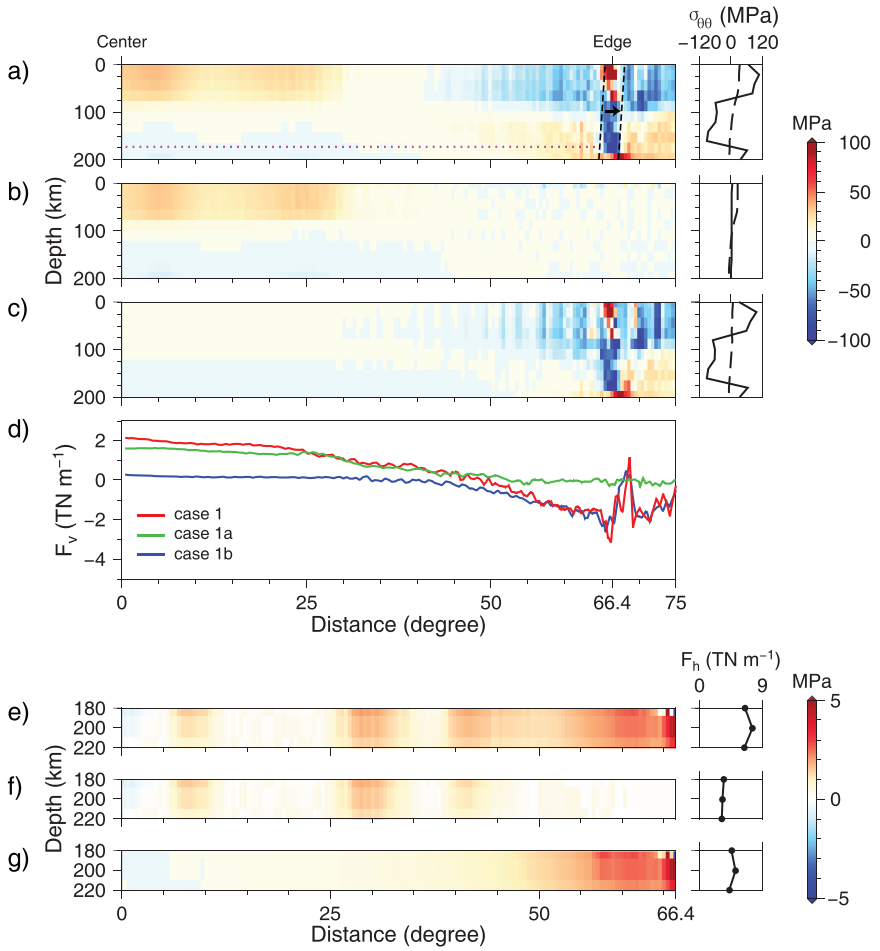

Figure 5. Normal stress states (positive values correspond to extension, while negative to compression) in supercontinent and its periphery (i.e., from supercontinent's center to 75° surrounding it) for (a) Case 1, (b) Case 1a, and (c) Case 1b at the breakup time. Their corresponding $\sigma_{\theta\theta}$ vs. depth profiles at the center (black dashed lines) and edge (black solid lines) of the supercontinent are shown in the right panel of (a)–(c). The area surrounded by dashed lines, the black arrow and the purple dot line in the left panel of (a) represent the region of weak zone, the direction of subduction retreat, and the bottom of continental lithosphere, respectively. The corresponding F_v vs. distance profiles for the three cases are given in (d). (e)-(g) show the shear stress states at 180–220 km depth of the supercontinent for Case 1, Case 1a, and Case 1b, respectively. The right panel of (e)-(g) give their corresponding F_h vs. depth profiles.

caused by the plume push toward a slowly expanding continental margin. The continental margin expands slower than our assigned rate of subduction retreat in this test case and thus becomes disconnected from the subduction girdle (see section 4.1 for discussion). A faster expanding continental margin that is attached to the subduction girdle would better compensate the effects of plume push, thus reducing the compressional force along the edge of the supercontinent.

To distinguish the relevant contributions of plume push and subduction retreat to the stress state, similar to Zhang et al. (2018), we carried out two more Stokes solutions using either (1) only the subcontinental hot structures (Figure 3f; Case 1a in Table 2) or (2) only the cold subduction slabs (Figure 3g; Case 1b in Table 2). The hot and cold structures were extracted separately from the temperature field of Case 1 (Figures 3d and 3e). We choose the division between hot structures and cold slabs following a 55° radius from the supercontinent center (black dashed lines in Figures 3e and 3f). The sum of these two Stokes solutions (Figures 5b and 5c) is broadly similar to the results of the reference case (Zhang et al., 2018). With only the hot plumes beneath the supercontinent, extension of the continental lithosphere occurs only in the interior 40° of the supercontinent (Figure 5b, and green line in Figure 5d). On the other hand, in the case with only the cold subduction retreat, negative stresses are shown at

Table 2
Test cases

Case no.	Temperature structure[a]	H	η_{ref} (Pa s)	η_c (C_2)[b]	Yield Stress[c]	Viscosity of weak zone (relative to the oceanic lithosphere)	Retreating rate (cm/year)
1	F	80	1×10^{22}	–	100 (4.06×10^{5})	1/30	2
1a	H	80	1×10^{22}	–	100 (4.06×10^{5})	1/30	2
1b	C	80	1×10^{22}	–	100 (4.06×10^{5})	1/30	2
1c	F	80	1×10^{22}	–	50 (2.03×10^{5})	1/30	2
1d	F	80	1×10^{22}	–	100 (4.06×10^{5})	1/30	1
1e	F	80	1×10^{22}	–	100 (4.06×10^{5})	1/100	2
1f	F	80	1×10^{22}	1/100	–	1/30	2
1g	H	80	1×10^{22}	1/100	–	1/30	2
1h	C	80	1×10^{22}	1/100	–	1/30	2
1i	F	80	1×10^{22}	–	100 (4.06×10^{5})	1/30	0
1j	F	80	1×10^{22}	1/100	–	1/30	0
2	F	0	1×10^{22}	–	100 (4.06×10^{5})	1/30	2
3	F	80	3×10^{21}	–	100 (1.35×10^{6})	1/30	2
4	F	80	3×10^{22}	–	100 (1.35×10^{5})	1/30	2

[a]If the thermal structure of a model is intact, it is F. H or C means the model contains only the resolved subcontinental hot plumes or the cold subduction slabs. [b]If the weaker orogens is omitted in the model, it is "–." Otherwise, it is a value showing the viscosity of orogens relative to that of continental lithosphere. [c]If the viscous yielding is omitted in the continents, it is "–." Otherwise, it is a number showing the yield stress (in MPa) in continents. The value in parentheses gives the yield stress in nondimensional form.

the supercontinent edge but with almost zero stress in the interior of the supercontinent (Figure 5c). The comparison of $\sigma_{\theta\theta}$ in the three cases suggests that the plume-push force dominates lithospheric extension in the interior of a homogeneous supercontinent.

The shear stress at the bottom of the supercontinent is generally positive above the plume heads, with a maximum value of ~5 MPa (Figure 5e) which is about one order of magnitude smaller than the plume-push induced normal stress in the center of the supercontinent (Figure 5b). The shear stress increases rapidly in the outer 10° of the supercontinent (right panel of Figure 5e), due to the significant velocity increase in the wedge corner flow induced by the subducted slab. The shear stress can also be decomposed into two independent Stokes solutions, which are shown in Figure 5f and 5g: that due to the subcontinental hot upwellings within 45° from the centre of the supercontinent (Figure 5f) and that due to the cold subducted slabs at the boundary of supercontinent (Figure 5g).

3.1.2. Integrated Total Forces

The dominance of plume-push effects in the extension of the supercontinent interior can be seen more clearly from the stress integrals of the three Stokes solutions: with only subcontinental hot upwelling structures, the integrated horizontal normal force F_v in the central region of supercontinent is ~1.8 TN/m (Figure 5d green line), comparable with F_v = ~2 TN/m (Figure 5d red line) in Case 1 where both the hot and cold structures are considered; the corresponding F_v is much lower if only cold subducted slabs are considered (~0.2 TN/m; Figure 5d blue line). The total extensional force contributed by cold subducted slabs focuses on the vicinity of the mantle wedge (Figure 5d blue line) but is negligible in the supercontinent interior.

On the other hand, the integrated horizontal shear force F_h at the base of supercontinent for these three Stokes calculations are ~8, ~3, and ~5 TN/m (Figures 5e–5g, right panel), respectively, suggesting the subcontinental plumes and the subduction girdle have similar contribution to the traction force at the bottom of the supercontinent.

3.1.3. Parameter Sensitivities

Based on the temperature field of the reference case at the breakup time, the sensitivities of normal and shear stresses to model parameters such as continental yield strength, trench retreat rate, and weak zone viscosity (Cases 1c–1e; Table 2) are examined. The stress states change a little compared with the reference case when these parameters are varied within the range considered here (Table 2). As an example, we show the $\sigma_{\theta\theta}$ and $\sigma_{r\theta}$ for the case using half of the reference continental yield stress (σ_y= 50 MPa, Case 1c) in Figure 6. The results show that extension concentrates in the inner 40° of the supercontinent (Figure 6a) and shear

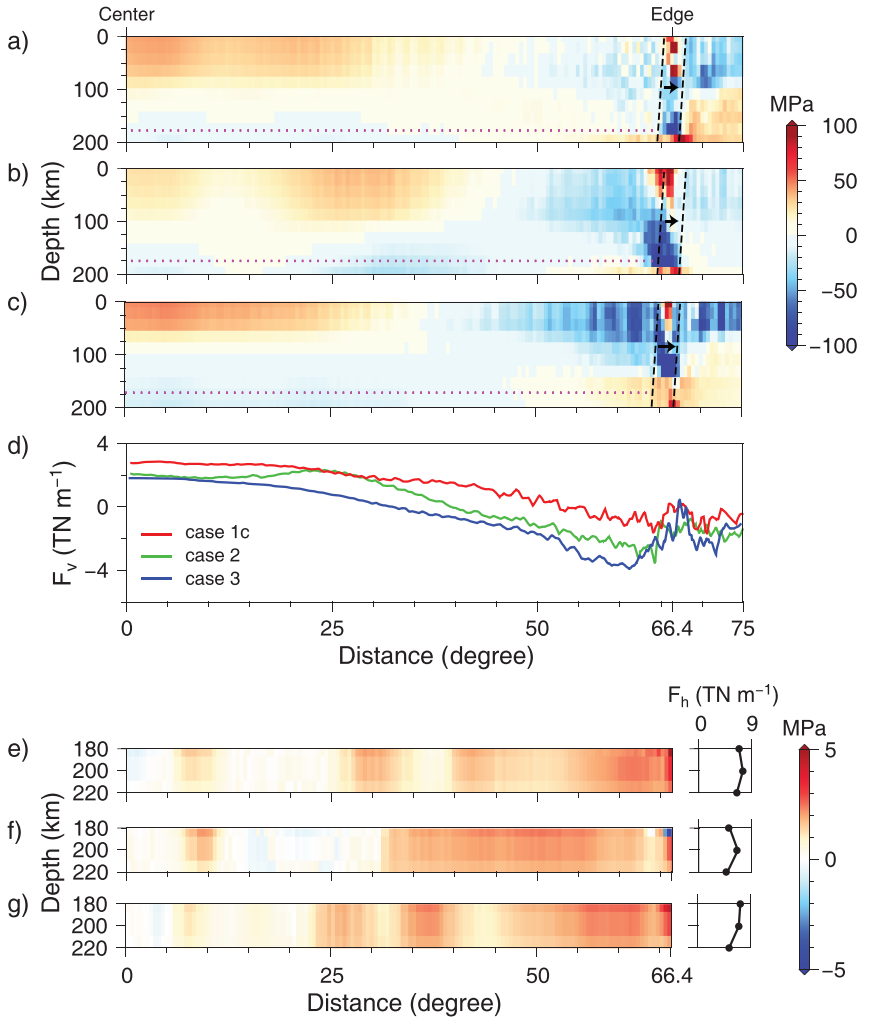

Figure 6. Normal stress states in supercontinent and its periphery for (a) Case 1c, (b) Case 2, and (c) Case 3. Their corresponding F_v vs. distance profiles are shown in (d). Panel (e)–(g) give the shear stress states at 180- to 220-km depth of the supercontinent for the three cases, respectively. The right panel of (e)–(g) show their corresponding F_h vs. depth profiles.

stress is almost always positive along the bottom of the supercontinent with values no larger than 5 MPa (Figure 6e). Both of them show patterns similar to Case 1 (Figure 5).

The influence of varying internal heating rate and reference viscosity/Rayleigh number (Cases 2–4, Table 2) on stress states is also tested here, although their initial temperature fields need to be recalculated beforehand (green, blue, and gray lines in Figure 1a). The results for the models with either no internal heating (Case 2) or ~3 times of Rayleigh number (Case 3) are shown in Figure 6. The magnitudes of both the extensional (Figures 6b and 6c) and shear stresses (Figures 6f and 6g) are comparable with that in the reference case (Figure 5). Differences only appear in the detailed distributions.

This insensitivity of the stress state to the controlling parameters can also be seen from the integrals F_v and F_h: the former fall in the range of 2–3 TN/m in the supercontinent interior (green and blue curves in Figure 6 d) and the latter ranges between 4 to 8 TN/m (Figures 6f and 6g, right panel) with changes in the parameters. Both are comparable with the reference case.

Although the correlation between the stress magnitudes and the Rayleigh number is weak in this work, they are suggested to be anti-correlated by previous studies (e.g., Lowman & Jarvis, 1995; Zhang et al., 2012). The weak dependence of stress on Rayleigh number here is probably caused by the hardly retreat slab wall (section 4.1) which limits the free deformation of continental blocks. In our test cases, a stable

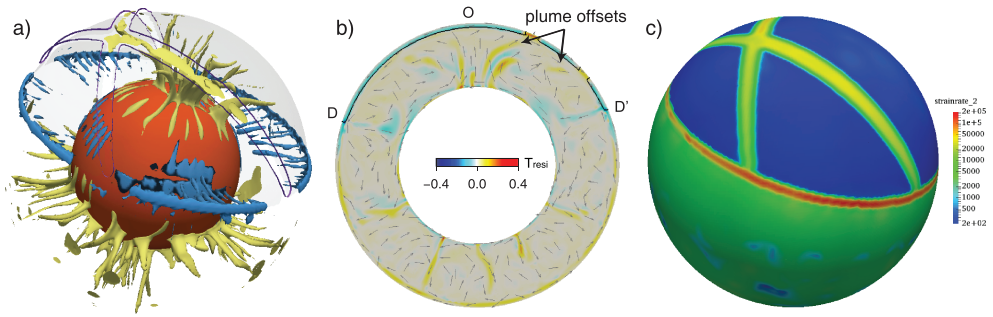

Figure 7. (a) 3-D presentation of the thermal structures (see caption of Figure 3 for details) for Case 1f at $t1$. The areas surrounding by purple lines in (a) denote the orogens. (b) The nondimensional residual temperature and velocity fields on the slice pass through $\hat{D}OD'$ in Figure 2. Note that the areas surrounded by black lines are continental blocks, and arrows point to orogen-induced plume offsets. The nondimensional second invariant of strain-rate at surface for Case 1f is given in (c). Here (a) and (c) share a same view-angle.

magnitude of stress is found in models with either 1/3 (Case 3) or 3 times (Case 4) of the reference viscosity profile (Figure 1b) following the viscosity range obtained by Mitrovica and Forte (2004). It suggests that in dynamic models with viscosity structures similar to the current mantle, and if plastic yielding occurs only in the continents, the extensional stress in the supercontinent at its breakup time is always around tens of MPa.

3.2. Stresses and Forces for a Supercontinent with Orogens

The stresses, especially $\sigma_{\theta\theta}$, may change significantly when orogens are introduced to the model supercontinent. For example, Case 1f shares similar conditions with Case 1 (i.e., the reference case in section 2.3) except that weak orogens are added to the supercontinent at time $t0$. Stresses of $\sigma_{\theta\theta}$ along two cross sections $\hat{B}OB'$ and $\hat{D}OD'$ (Figure 2) at time $t1$ (Figures 7a and 7b) are given in Figure 8. On each cross section, the extensional stress concentrates on the top 80 km of the continental lithosphere, with a large average value of ~160 MPa (Figures 8a and 8e), ~5 times of the stress values in the reference case. Such a stress magnitude is comparable with the results of Yoshida (2019). Particularly, in the orogens, the extensional stress reaches as large as 180 MPa, mostly focused onto the top 40 km of the lithosphere. This is because that once the week orogens start to stretch during the supercontinent breakup, they become thinner and underplated by the hot asthenospheric mantle (Figures 7a and 7b). Heat from the hot asthenospheric underplating dramatically decreases the viscosity of, and thus weakens, the orogens below 40 km depth (Figure 8). Such a high stress concentration in continents can also be seen from integrated horizontal force F_v, which is 2–8 TN/m, 1–4 times of the values when orogens are absent. However, F_v decreases to only 0–1.2 TN/m along orogens (Figures 8d and 8f). This indicates that the depth-averaged stress in orogens is less than that in continents, although the strain-rate concentrates in orogens (Figure 7c). Unlike Case 1, stress at the continental margin is extensional (5–50 MPa) in this situation, because the subducted slabs retreat more quickly than that in Case 1 (see section 4.1 for discussion). Although the weak orogens affect $\sigma_{\theta\theta}$ greatly, they do not show such effects on the basal shear stress (not shown).

Similar to section 3.1.1, two additional cases (Case 1g with only subcontinental hot structures and Case 1h with only cold subductions) based on Case 1f are tested, aiming to examine the relative importance of plume push vs. subduction retreat in the breakup of a orogens-embedded supercontinent. For the model with only subsupercontinent hot plumes, the resultant large extensional stress appears only in the inner 35–40° of the supercontinent (Figure 8b, and compare red and green lines in Figure 8d). On the other hand, the extensional force inside the supercontinent is neutral and only becomes large along the supercontinent margin when considering the subduction slabs only (Figures 8c and 8d, blue line). Our modeling of supercontinent breakup with orogens therefore suggests that plume push is still dominant in the breakup process.

3.3. Rapid Stress Decrease After the Breakup Time

In section 2.3, we used the maximum average extensional stress in shallow depths (0–40 km) of the continental lithosphere as a criterion to determine the breakup time of a supercontinent. To evaluate the longevity of

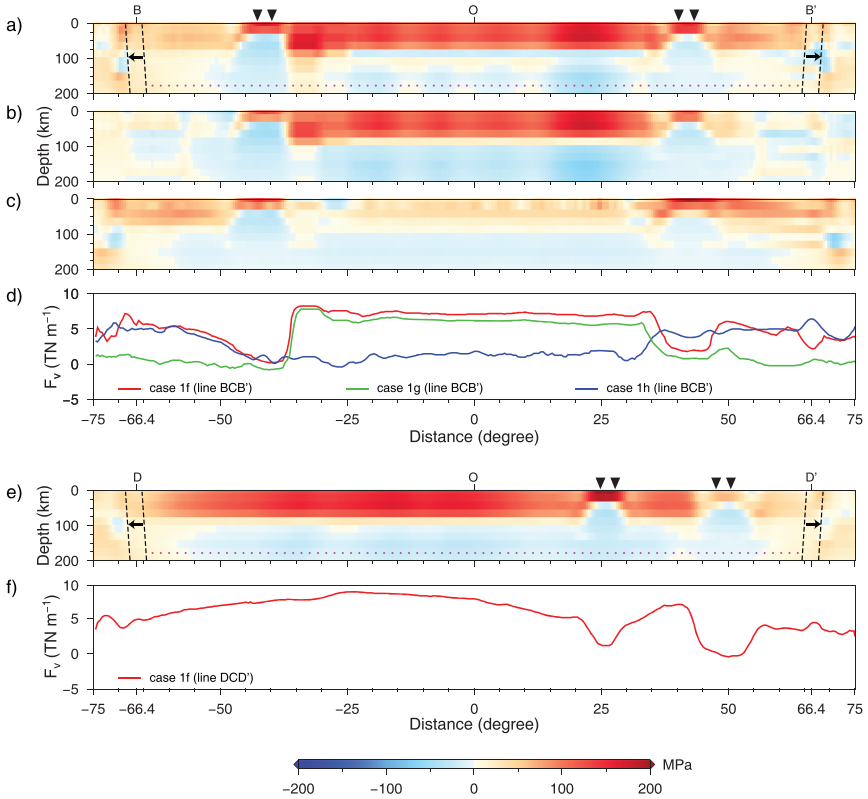

Figure 8. Normal stress states for (a) Case 1f, (b) Case 1g, and (c) Case 1h on cross section pass through arc $\hat{BOB'}$ (Figure 2) during the breakup time. (d) Their corresponding F_v vs. distance profiles. (e and f) The normal stress states and F_v vs. distance profile for Case 1f on section cross arc $\hat{DOD'}$ in Figure 2. Black triangles in (a) and (e) denote the positions of orogens.

stresses induced by the plumes, we conduct a calculation similar to Case 1 but with a fixed subduction girdle (Case 1i). The recorded stress (black line in Figure 3b) first increases from ~29 MPa at *t0* to ~44 MPa at *t1*, then decreases quickly in the next 40 Myr. For supercontinent with orogens (Case 1j), the analysis is restricted to a small region where two orogens intersect because the breakup first occurs here and its velocity field is divergent. The stress variation vs. time (blue line in Figure 3b) shows a pattern similar to that of Case 1i, i.e., the stress increases first then decreases after it reaches its peak at around *t1*, although the magnitude of the stress in Case 1j is ~3 times of that in Case 1i (Figure 3b). In both cases, ca. 40 Myr after the breakup time (*t1*), the stress drops to a level lower than that at *t0*. A drop of stress during initial supercontinent breakup was also observed in 2-D modeling by Ulvrova et al. (2019).

4. Discussions

4.1. Continental Dispersal: the Importance of Orogens

We define the time of supercontinent breakup as the time when the stress in the supercontinent reaches its maximum. Geological definition of continental breakup is generally the appearance of ocean floor between the breakapart continents, which should be slightly later than the maximum stress time. The evolution from the maximal extensional stress to the appearance of ocean floors corresponds to the transition from a slow continental extension to fast rifting (the rift-drift transition; e.g., Brune et al., 2016).

Although the spatial distribution of continental blocks after the breakup is not fully evaluated here, we nonetheless run Cases 1 and 1f for 50 Myr after the stress maximum is reached (i.e., after time *t1*) with a persistent rate of subduction retreat. In Case 1 we only allow a segment of the subduction boundary to retreat. This was because that we observe in our 3-D spherical geometry models that with a full slab wall (like Figure 3d) retreating at the same rate we are unable to produce boundary extension (Figure 9) as observed in the

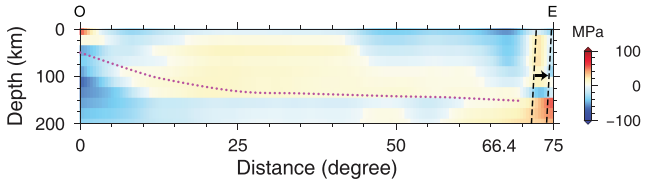

Figure 9. Normal stress state in supercontinent and its periphery at $t1 + 50$ Myr for Case 1 with a subduction girdle.

present-day back-arc regions (more in section 4.5). This may have been caused by mass imbalance when the wall of the retreating slab seals the subsupercontinent mantle and thus disallows external mantle materials to flow in. However, this difficulty does not apply to Case 1f because its subduction girdle is segmented at the ends of the orogen. Here, we just allow the subduction retreat to occur at a ~2,000-km-long subduction zone (white segment in Figure 10a; Schellart et al., 2007).

Case 1 at 50 Myr after $t1$ shows extension at the continental boundary bounded by the 2000-km retreating subduction zone. A strain concentration beyond the original continental margin near the 2000-km-long trench (white dashed line in Figure 10 b) can also be seen. However, we observe no Earth-like dispersal in Case 1, but broad zones of thinning at the bottom of the supercontinent's interior regions (Figure 10b). By contrast, the dispersal of continent blocks in Case 1f shows behaviors more consistent with observed continental drift (Figures 10d and 10e). The different deformation behaviors (Figures 10b vs. 10e) during breakup suggest that supercontinents with week zones (orogens) promote more plate-like continental drift (Lenardic et al., 2003; Yoshida, 2013).

4.2. Stress Evolution After Supercontinent Breakup

Besides the dispersal of continental blocks, the normal stress $\sigma_{\theta\theta}$ for the above two models after a persistent ~50 Myr subduction retreat are also examined (Figures 10c and 10f). Both the homogeneous and orogen-embedded supercontinent models show an extensional state (~20 MPa for the former, and 5–50 MPa for the latter) at the continental margin near the subduction zone, which is consistent with the extensional continental margin observed in the present-day circum-Pacific subduction zones (except for the Andes) and predicted by previous models of subduction retreat (e.g., Dal Zillo et al., 2018; Yoshida, 2017). We also observe a significant decrease in the magnitude of $\sigma_{\theta\theta}$ in the interiors of supercontinent approximately 50 Myr after the supercontinent breakup time ($t1$) and with subduction retreat: 20–50 MPa in model with homogeneous supercontinent (comparing Figures 5a and 10c) and 40–100 MPa in model with orogens (comparing Figure 10f's top and bottom panels). This suggests that once supercontinent breakup is initiated, the subsequent sea-floor spreading may operate at much smaller stress environment.

After the breakup point, the stress in the continents drops to 30–90 MPa (Figure 10f's bottom panel) which is below the continental strength (100 MPa in this work). Such a stress drop prevents large deformation in the continental interior, and thus ensures the stability of continent blocks during continental drift. Since the hot upwellings continue to contribute to the convection cells beneath the continents even after the breakup (Morgan, 1972; Wilson, 1973), the traction force generated by the convection cells likely acts as the primary driving force for the continental drifts (Yoshida & Hamano, 2015; Yoshida & Santosh, 2018).

4.3. Doming by Plume Cluster and Gravitational Collapse Force During the Breakup

Our free-slip boundary model does not consider the surface high topography induced by the mantle plume cluster (superplume, or superupwelling). A surface doming can lead to a gravitational collapse, which can contribute to the supercontinent breakup (Bercovici & Long, 2014; Li, 2014). Although our model cannot explicitly compute the collapse of such a continental mass, modeling of such forces due to dynamic topography has previously been attempted (Zhang et al., 2012; Zhong & Zuber, 2000). Moreover, the continent mass collapse force is relatively small compared to the force by the slab rollback (Bercovici & Long, 2014).

4.4. Influences of Simplified Lithospheric Strength

This study did not use layered (e.g., upper crust, lower crust, and lithospheric mantle) continental lithosphere. Although having a layered continental lithosphere is important for regional modeling (e.g., Brune et al., 2016), our study focuses on the stress magnitudes and their integrals on a global scale. The effect of such simplification on strength profile needs further examination in future studies. However, we believe that our main results on the global-scale processes are robust.

4.5. Length of Subduction Zone and the Speed of Continuous Subduction Retreat During the Breakup

Our global model prefers a discontinuous slab wall with gaps, to allow for mass balance between the two sides of the subduction girdle. Hence, we modeled the retreating of a ~2000-km wide subduction zone in

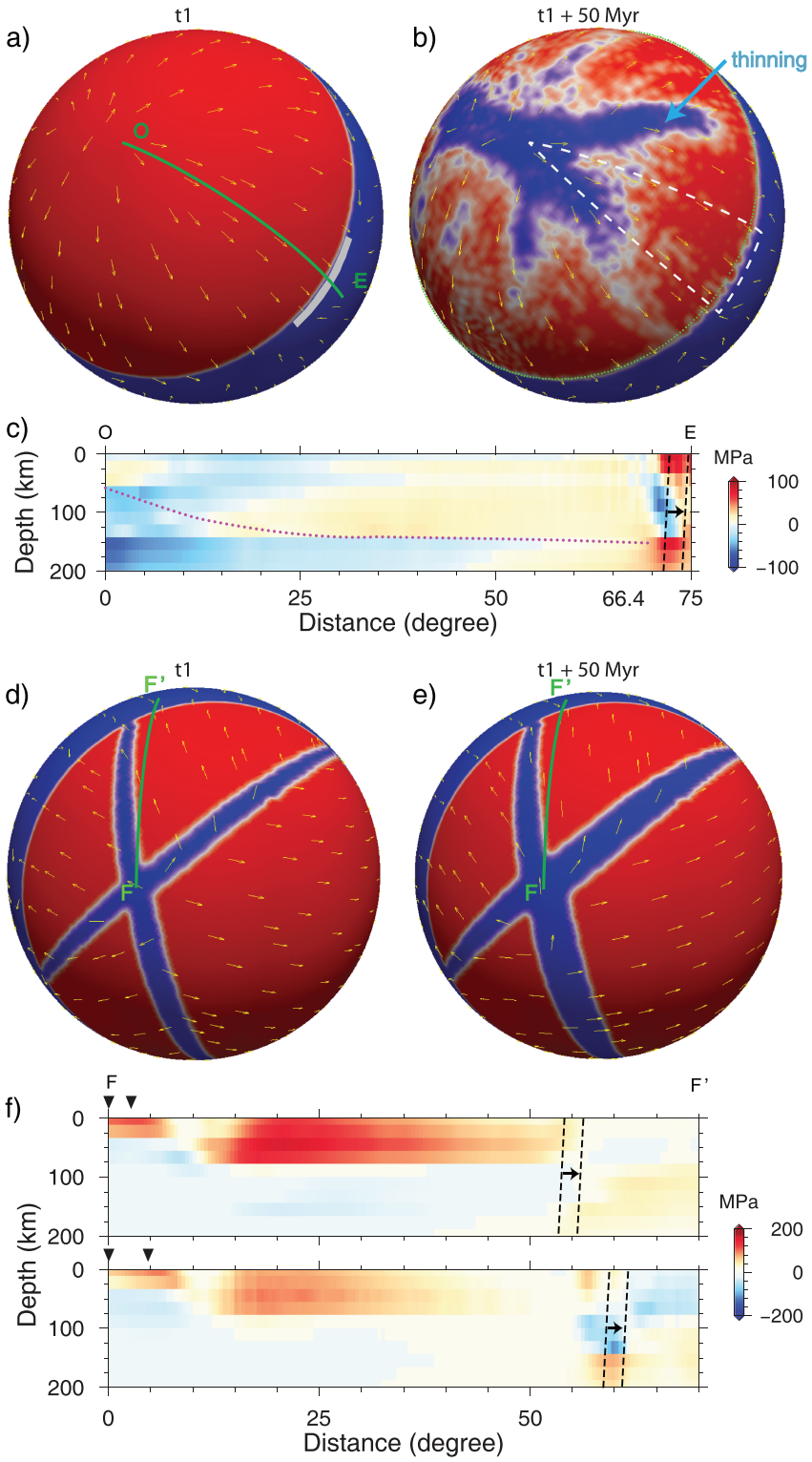

Figure 10. Composition (red for continental lithosphere, blue for sub-lithospheric mantle) and velocity fields for Case 1 at 160-km depth (a) at $t1$ and (b) 50 Myr after the inception of subduction retreat. The gray area in (a) is the ~2,000-km wide retreating slab mentioned in section 4.1. The green dot line in (b) denotes the supercontinent boundary at $t1$, and the area surrounded by white dash lines is the region where strain concentrates due to the subduction retreat. (c) The normal stress state in supercontinent along arc $\hat{OE}$ in (a) for Case 1 at $t1$ + 50 Myr, in which the purple dot line shows the bottom of the continental lithosphere. (d and e) The composition (red for continental lithosphere, blue for sub-lithospheric mantle under orogens) and velocity fields for Case 1f at 160-km depth at time $t1$ and $t1$ + 50 Myr, respectively. (f) The extensional stresses for Case 1f at $t1$ (top panel) and $t1$ + 50 Myr (bottom panel) on cross-section passing through $\hat{FF'}$ in (d) and (e). The black triangles in (f) denote the positions of orogens.

Table A1
Test Cases for the Hot Patterns Below Supercontinent

Case no.	Single plume[a]	Plume annular wall[a]
A1	0–17° (150 K)	–
A2	–	22–28° (150 K)
A3	0–22° (20 K)	22–24° (150 K) 24–55° (10 K)

[a]If the plume/plume-wall is omitted in the model, it is "–."

Case 1 because the retreating of sealed subduction girdle is unrealistic. Future modeling of such processes may introduce stringy subduction slabs instead of a continuous and sealed subducting slab.

Also, the subduction retreat observed in the present-day Earth shows an anti-correlation between the average retreating rate and the length of a subduction slab (Schellart et al., 2007). It is obvious that a shorter subduction zones can lead to a faster retreating rate, and therefore a more clear extension at continental margins. In this study, the manually specified subduction retreat rate may cause trench-continent disconnections at certain segments of subduction zones, because the continental boundary may not always follow the retreating trenches. Although long-term drifting of continental plates after supercontinent breakup is beyond of our current model, it has been investigated in other studies (Rolf et al., 2018; Yoshida & Santosh, 2014).

5. Conclusions

We have formulated 3-D spherical mantle convection models with a supercontinent of different mechanical properties (i.e., homogeneous or with weak orogens). Using the models, we investigate generation and growth of subsupercontinent hot upwelling plumes in response to circum-supercontinent subduction, the effects of these hot plumes and cold slabs on stress state in the supercontinent, and their impact on supercontinent breakup. Our modeling results are summarized as follows.

1. In our models, during the breakup of a homogenous supercontinent (i.e., without orogens or weak zones), the inner region of the supercontinent is subjected to extensional stress of 20–50 MPa resulting in defused zones of lithospheric thinning and plastic yielding.
2. We modeling suggests that with the existence of weak orogens, the plume push stresses can reach average values of ~160 and ~180 MPa in the top 80 km of the cratonic blocks and the top 40 km of the orogens, respectively. The integrated horizontal force for continents is 2–8 TN/m whereas it is only 0–1.2 TN/m in the weak orogens prior to the breakup along the orogens.
3. The subsupercontinent hot upwellings are the dominant driving mechanism for extension in the supercontinent interiors, whereas the stress at the supercontinental margin is more influenced by the retreat of the subduction system.
4. Only supercontinent with orogens can generate plate-like continental breakup and dispersion.

Appendix: Pattern of Subsupercontinent Hot Structures A

The configuration of plume structures (i.e., thermal state) during the supercontinent breakup is widely debated. Regularly, the plume cluster during supercontinent breakup is regarded to be beneath the supercontinent center. However, the reconstruction of large igneous provinces (LIPs; Burke et al., 2008) shows that the present-day plume heads are in fact circling around the two LLSVPs. Obviously, different spatial distribution of plumes under a supercontinent can lead to different stress distribution and thus different geometry of supercontinental breaking-up. The generation of self-consistent subsupercontinent hot structures in this study is in the first order consistent with that of Burke et al. (2008), and it therefore allows us to more realistically evaluate the stress distribution during supercontinent dispersal.

To examine the difference in terms of stress states and breakup locations, we set up three hypothetical plume structures (Table A1 and Figure A1) here. These plume structures are based on the average subsupercontinent thermal state of the reference case, which is ~15 K higher than that in the mantle outside the supercontinent. The hypothetical hot structures are used to replace the self-consistently generated hot structure of our model (i.e., comparable in stress states). Each of hypothetical plume structures represents different characteristics of hot structures.

The first hot structure is a single "plume" right below the supercontinent central region. Its excess temperature is 150 K based on the evaluated plume temperature beneath Hawaii (Agius et al., 2017), which can be taken as the lower limit of plume excess temperature. Converting the average subsupercontinent hot anomaly of 15 K to a "plume" with excess temperature 150 K, we obtain a "plume" with 17° radius (Case A1, Figure A1a). In this case, intensive extensional stress occurs in inner ~17° of supercontinent with maximal

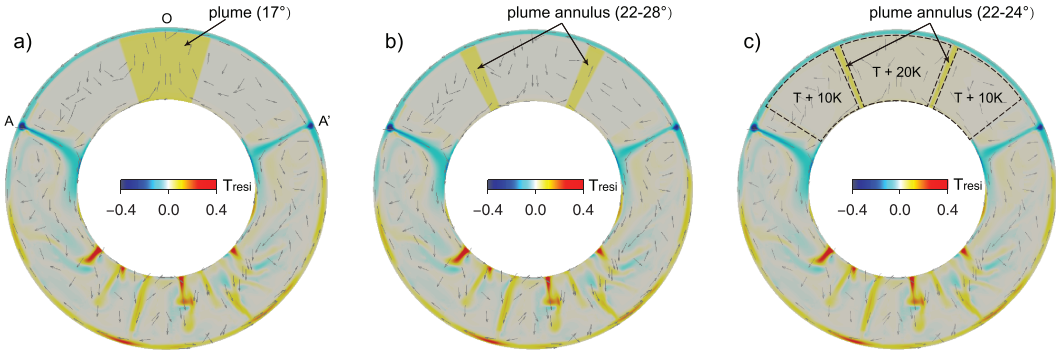

Figure A1. Nondimensional residual temperature and velocity fields for (a) Case A1, (b) Case A2, and (c) Case A3 in cross section pass through arc $\overset{\frown}{AOA'}$ in Figure 3d.

exceeding 100 MPa (Figure A2a); outside the ~17°, the continent blocks are in compression (Figure A2a). The maximal F_v in central supercontinent and F_h in lithospheric bottom are −6 and 35 TN/m (Figure A2d red curve and Figure A2e), respectively, far larger than those of the reference case. The second hot structure

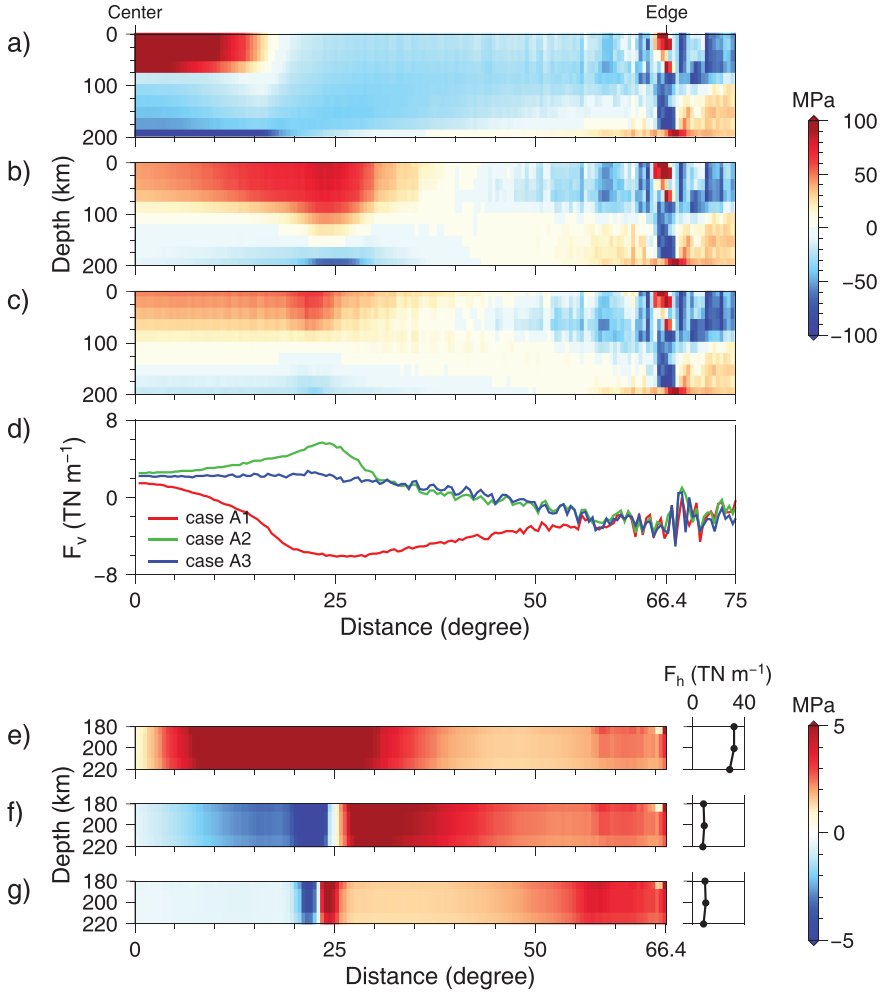

Figure A2. Normal stress states in supercontinent and its periphery for (a) Case A1, (b) Case A2, and (c) Case A3 with (d) their corresponding F_v vs. distance profiles. (e–g) The shear stress states in supercontinent bottom as well as the integration F_h vs. depth profiles for the three cases, respectively.

we tested (Case A2, Figure A1b) is a plume-cluster-like annular wall. Now, we convert the total heat budget beneath the supercontinent to an annular wall with an excess temperature of 150 K, which gives rise to a 6° wide annular wall. We choose the inner and outer radii of this wall at 22° (the average distance of reconstructed LIPs around the LLSVP beneath Africa) and 28° away from the supercontinent center. Stress state in this case shows extension in the inner 35° of continent blocks, but reaches as large as 100 MPa at ~25° where F_v is ~6 TN/m (Figure A2b and the green curve in Figure A2d) and about two times of the magnitude of Case 1, also showing obvious discrepancy with the reference case.

The above two tests suggest that in order to match the stress states predicted by the self-consistent supercontinent model (Case 1), the subsupercontinent hot structure can neither be a single "plume" only nor a plume annulus only. They both cause too big stress magnitude and cannot lead to an extensional stress enough outside the annulus, although the resultant stress in the plume annulus case is similar to that in Case 1. The possible structure needs to induce more extensional stress outside the annular wall and low the magnitude down. After tuning the temperatures inside and outside of the annulus, we found our preferred model (Case A3). In this model, the hot structure contains a plume annulus of 2° width, which is the regular size of present-day plume heads (Campbell & Griffiths, 1990; Courtillot et al., 1999). Inside the annulus, there is a plume of 22° width with extra average temperature of 20 K; beyond the outside boundary of annulus at 24°, the extra average temperature is 10 K (Figure A1c). Stress state in this model is much similar to the reference case in both stress distribution and integrals F_v and F_h (Figure A2c; blue curve in Figures A2d and A2g) despite the rapid shear stress change at the boundaries of plume annulus (i.e., quick decrease and increase on the thermal gradients of annulus; Figure A2g) caused by the temperature jumps in there. These results suggest that substantial portion of heat energy is scattered in the mantle rather than just concentrates in plumes (or plume cluster).

Acknowledgments
We thank Tobias Rolf and Masaki Yoshida for their thoughtful comments. Careful reading by Thorsten Becker helps improving of the manuscript. We also want to thank the discussions with our colleagues of Earth Dynamics Group. This work was supported by Australian Research Council Australian Laureate Fellowship grant to Z. X. L. (FL150100133), by China's Thousand Talents Plan (2016) and NSFC 41674098 to N. Z., and by U.S. NSF (grant 1645245) to S. Z. Computational Infrastructure for Geodynamics is thanked for distributing the software CitcomS (https://geodynamics.org/cig/software/citcoms/) that is used in this study. Computational work was supported by resources provided by the High-performance Computing Platform of Peking University and the Pawsey Supercomputing Centre with funding from the Australian Government and the Government of Western Australia. This is CCFS contribution 1033, and a contribution to IGCP 648.

References

Agius, M. R., Rychert, C. A., Harmon, N., & Laske, G. (2017). Mapping the mantle transition zone beneath Hawaii from Ps receiver functions: Evidence for a hot plume and cold mantle downwellings. *Earth and Planetary Science Letters*, *474*, 226–236. https://doi.org/10.1016/j.epsl.2017.06.033

Bercovici, D., & Long, M. D. (2014). Slab rollback instability and supercontinent dispersal. *Geophysical Research Letters*, *41*, 6659–6666. https://doi.org/10.1002/2014GL061251

Bleeker, W. (2003). The late Archean record: A puzzle in ca. 35 pieces. *Lithos*, *71*(2-4), 99–134. https://doi.org/10.1016/j.lithos.2003.07.003

Bradley, D. C. (2011). Secular trends in the geologic record and the supercontinent cycle. *Earth-Science Reviews*, *108*(1-2), 16–33. https://doi.org/10.1016/j.earscirev.2011.05.003

Brune, S., Williams, S. E., Butterworth, N. P., & Müller, R. D. (2016). Abrupt plate accelerations shape rifted continental margins. *Nature*, *536*(7615), 201–204. https://doi.org/10.1038/nature18319

Buiter, S. J. H., & Torsvik, T. H. (2014). A review of Wilson Cycle plate margins: A role for mantle plumes in continental break-up along sutures? *Gondwana Research*, *26*(2), 627–653. https://doi.org/10.1016/j.gr.2014.02.007

Burke, K., Steinberger, B., Torsvik, T. H., & Smethurst, M. A. (2008). Plume Generation Zones at the margins of Large Low Shear Velocity Provinces on the core-mantle boundary. *Earth and Planetary Science Letters*, *265*(1–2), 49–60. https://doi.org/10.1016/j.epsl.2007.09.042

Campbell, I. H., & Griffiths, R. W. (1990). Implications of mantle plume structure for the evolution of flood basalts. *Earth and Planetary Science Letters*, *99*(1-2), 79–93. https://doi.org/10.1016/0012-821X(90)90072-6

Cande, S. C., & Stegman, D. R. (2011). Indian and African plate motions driven by the push force of the Reunion plume head. *Nature*, *475*(7354), 47–52. https://doi.org/10.1038/nature10174

Collins, W. J. (2003). Slab pull, mantle convection, and Pangaean assembly and dispersal. *Earth and Planetary Science Letters*, *205*(3-4), 225–237. https://doi.org/10.1016/S0012-821X(02)01043-9

Courtillot, V., Jaupart, C., Manighetti, I., Tapponnier, P., & Besse, J. (1999). On causal links between flood basalts and continental breakup. *Earth and Planetary Science Letters*, *166*(3-4), 177–195. https://doi.org/10.1016/S0012-821X(98)00282-9

Dal Zilio, L., Faccenda, M., & Capitanio, F. (2018). The role of deep subduction in supercontinent breakup. *Tectonophysics*, *746*, 312–324. https://doi.org/10.1016/j.tecto.2017.03.006

Dietz, R. S., & Holden, J. C. (1970). Reconstruction of Pangaea: Breakup and dispersion of continents, Permian to Present. *Journal of Geophysical Research*, *75*(26), 4939–4956. https://doi.org/10.1029/JB075i026p04939

Flament, N., Gurnis, M., Williams, S., Seton, M., Skogseid, J., Heine, C., & Dietmar Müller, R. (2014). Topographic asymmetry of the South Atlantic from global models of mantle flow and lithospheric stretching. *Earth and Planetary Science Letters*, *387*, 107–119. https://doi.org/10.1016/j.epsl.2013.11.017

Foley, B. J., & Becker, T. W. (2009). Generation of plate-like behavior and mantle heterogeneity from a spherical, viscoplastic convection model. *Geochemistry, Geophysics, Geosystems*, *10*, Q08001. https://doi.org/10.1029/2009GC002378

Gung, Y., Panning, M., & Romanowicz, B. (2003). Global anisotropy and the thickness of continents. *Nature*, *422*(6933), 707–711. https://doi.org/10.1038/nature01559

Gurnis, M. (1988). Large-scale mantle convection and the aggregation and dispersal of supercontinents. *Nature*, *332*(6166), 695–699. https://doi.org/10.1038/332695a0

Heine, C., Zoethout, J., & Müller, R. D. (2013). Kinematics of the South Atlantic rift. *Solid Earth*, *4*(2), 215–253. https://doi.org/10.5194/se-4-215-2013

Heron, P. J., Lowman, J. P., & Stein, C. (2015). Influences on the positioning of mantle plumes following supercontinent formation. *Journal of Geophysical Research: Solid Earth*, *120*, 3628–3648. https://doi.org/10.1002/2014jb011727

Holbrook, W. S., Reiter, E. C., Purdy, G. M., Sawyer, D., Stoffa, P. L., Austin, J. A. Jr., et al. (1994). Deep structure of the U.S. Atlantic continental margin, offshore South Carolina, from coincident ocean bottom and multichannel seismic data. *Journal of Geophysical Research - Solid Earth*, *99*(B5), 9155–9178. https://doi.org/10.1029/93jb01821

Holt, A. F., Becker, T. W., & Buffett, B. A. (2015). Trench migration and overriding plate stress in dynamic subduction models. *Geophysical Journal International*, *201*(1), 172–192. https://doi.org/10.1093/gji/ggv011

Hyndman, R. D., Currie, C. A., & Mazzotti, S. P. (2005). Subduction zone backarcs, mobile belts, and orogenic heat. *GSA Today*, *15*(2), 4–10. https://doi.org/10.1130/1052-5173(2005)015<4:SZBMBA>2.0.CO;2

Kamo, S. L., Czamanske, G. K., & Krogh, T. E. (1996). A minimum U-Pb age for Siberian flood-basalt volcanism. *Geochimica et Cosmochimica Acta*, *60*(18), 3505–3511. https://doi.org/10.1016/0016-7037(96)00173-1

Kohlstedt, D. L., Evans, B., & Mackwell, S. J. (1995). Strength of the lithosphere: Constraints imposed by laboratory experiments. *Journal of Geophysical Research - Solid Earth*, *100*(B9), 17,587–17,602. https://doi.org/10.1029/95JB01460

Koptev, A., Calais, E., Burov, E., Leroy, S., & Gerya, T. (2015). Dual continental rift systems generated by plume–lithosphere interaction. *Nature Geoscience*, *8*(5), 388–392. https://doi.org/10.1038/ngeo2401

Lenardic, A., Moresi, L. N., & Mühlhaus, H. (2003). Longevity and stability of cratonic lithosphere: Insights from numerical simulations of coupled mantle convection and continental tectonics. *Journal of Geophysical Research - Solid Earth*, *108*(B6). https://doi.org/10.1029/2002JB001859

Li, Z.X., 2014. Supercontinent break-up: Causes and consequences. In: AGU Fall Meeting. San Francisco, CA. T33Be4655.

Li, Z. X., Bogdanova, S. V., Collins, A. S., Davidson, A., De Waele, B., Ernst, R. E., et al. (2008). Assembly, configuration, and breakup history of Rodinia: A synthesis. *Precambrian Research*, *160*(1-2), 179–210. https://doi.org/10.1016/j.precamres.2007.04.021

Li, Z. X., Li, X. H., Kinny, P. D., & Wang, J. (1999). The breakup of Rodinia: Did it start with a mantle plume beneath South China? *Earth and Planetary Science Letters*, *173*(3), 171–181. https://doi.org/10.1016/S0012-821X(99)00240-X

Li, Z. X., & Zhong, S. (2009). Supercontinent-superplume coupling, true polar wander and plume mobility: Plate dominance in whole-mantle tectonics. *Physics of the Earth and Planetary Interiors*, *176*(3-4), 143–156. https://doi.org/10.1016/j.pepi.2009.05.004

Lowman, J. P., & Jarvis, G. T. (1995). Mantle convection models of continental collision and breakup incorporating finite thickness plates. *Physics of the Earth and Planetary Interiors*, *88*(1), 53–68. https://doi.org/10.1016/0031-9201(94)05076-A

Lu, G., Kaus, B. J. P., Zhao, L., & Zheng, T. (2015). Self-consistent subduction initiation induced by mantle flow. *Terra Nova*, *27*(2), 130–138. https://doi.org/10.1111/ter.12140

Mallard, C., Coltice, N., Seton, M., Müller, R. D., & Tackley, P. J. (2016). Subduction controls the distribution and fragmentation of Earth's tectonic plates. *Nature*, *535*(7610), 140–143. https://doi.org/10.1038/nature17992

McNamara, A. K., & Zhong, S. (2004). Thermochemical structures within a spherical mantle: Superplumes or piles? *Journal of Geophysical Research - Solid Earth*, *109*(B7), 1–14. https://doi.org/10.1029/2003JB002847

Mitrovica, J. X., & Forte, A. M. (2004). A new inference of mantle viscosity based upon joint inversion of convection and glacial isostatic adjustment data. *Earth and Planetary Science Letters*, *225*(1-2), 177–189. https://doi.org/10.1016/j.epsl.2004.06.005

Morgan, W. J. (1972). Deep mantle convection plumes and plate motions. *AAPG Bulletin*, *56*(2), 203–213.

Neumann, E. R., Olsen, K. H., Baldridge, W. S., & Sundvoll, B. (1992). The Oslo Rift: A review. *Tectonophysics*, *208*(1-3), 1–18. https://doi.org/10.1016/0040-1951(92)90333-2

Nyblade, A. A., & Robinson, S. W. (1994). The African Superswell. *Geophysical Research Letters*, *21*(9), 765–768. https://doi.org/10.1029/94GL00631

Phillips, B. R., & Bunge, H.-P. (2007). Supercontinent cycles disrupted by strong mantle plumes. *Geology*, *35*(9), 847–850. https://doi.org/10.1130/g23686a.1

Poudjom Djomani, Y. H., O'Reilly, S. Y., Griffin, W. L., & Morgan, P. (2001). The density structure of subcontinental lithosphere through time. *Earth and Planetary Science Letters*, *184*(3-4), 605–621. https://doi.org/10.1016/S0012-821X(00)00362-9

Reddy, J. N. (2013). *An introduction to continuum mechanics*. UK: Cambridge university press.

Rivers, T. (2015). Tectonic setting and evolution of the Grenville Orogen: An assessment of progress over the last 40 years. *Geoscience Canada*, *42*(1), 77–124. https://doi.org/10.12789/geocanj.2014.41.057

Rogers, J. J. W., & Santosh, M. (2003). Supercontinents in Earth History. *Gondwana Research*, *6*(3), 357–368. https://doi.org/10.1016/S1342-937X(05)70993-X

Rolf, T., Capitanio, F. A., & Tackley, P. J. (2018). Constraints on mantle viscosity structure from continental drift histories in spherical mantle convection models. *Tectonophysics*, *746*, 339–351. https://doi.org/10.1016/j.tecto.2017.04.031

Rolf, T., Coltice, N., & Tackley, P. J. (2012). Linking continental drift, plate tectonics and the thermal state of the Earth's mantle. *Earth and Planetary Science Letters*, *351-352*, 134–146. https://doi.org/10.1016/j.epsl.2012.07.011

Rolf, T., Coltice, N., & Tackley, P. J. (2014). Statistical cyclicity of the supercontinent cycle. *Geophysical Research Letters*, *41*, 2351–2358. https://doi.org/10.1002/2014gl059595

Rolf, T., & Tackley, P. J. (2011). Focussing of stress by continents in 3D spherical mantle convection with self-consistent plate tectonics. *Geophysical Research Letters*, *38*, L18301. https://doi.org/10.1029/2011GL048677

Schellart, W. P., Freeman, J., Stegman, D. R., Moresi, L., & May, D. (2007). Evolution and diversity of subduction zones controlled by slab width. *Nature*, *446*(7133), 308–311. https://doi.org/10.1038/nature05615

Schellart, W. P., Stegman, D. R., & Freeman, J. (2008). Global trench migration velocities and slab migration induced upper mantle volume fluxes: Constraints to find an Earth reference frame based on minimizing viscous dissipation. *Earth-Science Reviews*, *88*(1-2), 118–144. https://doi.org/10.1016/j.earscirev.2008.01.005

Seton, M., Müller, R. D., Zahirovic, S., Gaina, C., Torsvik, T., Shephard, G., et al. (2012). Global continental and ocean basin reconstructions since 200 Ma. *Earth-Science Reviews*, *113*(3–4), 212–270. https://doi.org/10.1016/j.earscirev.2012.03.002

Storey, B. C. (1995). The role of mantle plumes in continental breakup: Case histories from Gondwanaland. *Nature*, *377*(6547), 301–308. https://doi.org/10.1038/377301a0

Tackley, P. J. (2000). Self-consistent generation of tectonic plates in time-dependent, three-dimensional mantle convection simulations. *Geochemistry, Geophysics, Geosystems*, *1*(8). https://doi.org/10.1029/2000GC000036

Tackley, P. J., & King, S. D. (2003). Testing the tracer ratio method for modeling active compositional fields in mantle convection simulations. *Geochemistry, Geophysics, Geosystems*, *4*(4), 8302. https://doi.org/10.1029/2001GC000214

Torsvik, T. H., Rousse, S., Labails, C., & Smethurst, M. A. (2009). A new scheme for the opening of the South Atlantic Ocean and the dissection of an Aptian salt basin. *Geophysical Journal International*, *177*(3), 1315–1333. https://doi.org/10.1111/j.1365-246X.2009.04137.x

Tupinambá, M., Heilbron, M., Ragatky, D., & Machado, N. (2007). Meso-neoproterozoic lithospheric extensional events in the Sao Francisco Craton and its surrounding south American and African metamorphic belts: A compilation of U-Pb ages. *Revista Brasileira de Geociencias*, *37*(S4), 87–91. https://doi.org/10.25249/0375-7536.200737S48791

Turcotte, D. L., & Schubert, G. (2014). *Geodynamics*. UK: Cambridge University Press.

Ulvrova, M. M., Brune, S., & Williams, S. (2019). Breakup Without Borders: How Continents Speed Up and Slow Down During Rifting. *Geophysical Research Letters*, *46*(3), 1338–1347. https://doi.org/10.1029/2018gl080387

Veevers, J. J. (2004). Gondwanaland from 650–500 Ma assembly through 320 Ma merger in Pangea to 185–100 Ma breakup: Supercontinental tectonics via stratigraphy and radiometric dating. *Earth-Science Reviews*, *68*(1-2), 1–132. https://doi.org/10.1016/j.earscirev.2004.05.002

Wilson, J. T. (1973). Mantle plumes and plate motions. *Tectonophysics*, *19*(2), 149–164. https://doi.org/10.1016/0040-1951(73)90037-1

Yoshida, M. (2013). Mantle temperature under drifting deformable continents during the supercontinent cycle. *Geophysical Research Letters*, *40*, 681–686. https://doi.org/10.1002/grl.50151

Yoshida, M. (2014). Effects of various lithospheric yield stresses and different mantle-heating modes on the breakup of the Pangea supercontinent. *Geophysical Research Letters*, *41*, 3060–3067. https://doi.org/10.1002/2014GL060023

Yoshida, M. (2017). Trench dynamics: Effects of dynamically migrating trench on subducting slab morphology and characteristics of subduction zones systems. *Physics of the Earth and Planetary Interiors*, *268*(Supplement C), 35–53. https://doi.org/10.1016/j.pepi.2017.05.004

Yoshida, M. (2019). On mantle drag force for the formation of a next supercontinent as estimated from a numerical simulation model of global mantle convection. *Terra Nova*, *31*(2), 135–149. https://doi.org/10.1111/ter.12380

Yoshida, M. (2010). Temporal evolution of the stress state in a supercontinent during mantle reorganization. *Geophysical Journal International*, *180*(1), 1–22. https://doi.org/10.1111/j.1365-246X.2009.04399.x

Yoshida, M., & Hamano, Y. (2015). Pangea breakup and northward drift of the Indian subcontinent reproduced by a numerical model of mantle convection. *Scientific Reports*, *5*, 8407. https://doi.org/10.1038/srep08407

Yoshida, M., & Santosh, M. (2011). Supercontinents, mantle dynamics and plate tectonics: A perspective based on conceptual vs. numerical models. *Earth-Science Reviews*, *105*(1-2), 1–24. https://doi.org/10.1016/j.earscirev.2010.12.002

Yoshida, M., & Santosh, M. (2014). Mantle convection modeling of the supercontinent cycle: Introversion, extroversion, or a combination? *Geoscience Frontiers*, *5*(1), 77–81. https://doi.org/10.1016/j.gsf.2013.06.002

Yoshida, M., & Santosh, M. (2018). Voyage of the Indian subcontinent since Pangea breakup and driving force of supercontinent cycles: Insights on dynamics from numerical modeling. *Geoscience Frontiers*, *9*(5), 1279–1292. https://doi.org/10.1016/j.gsf.2017.09.001

Zhang, C.-L., Li, Z. X., Li, X.-H., Xu, Y.-G., Zhou, G., & Ye, H.-M. (2010). A Permian large igneous province in Tarim and Central Asian orogenic belt, NW China: Results of a ca. 275 Ma mantle plume? *GSA Bulletin*, *122*(11–12), 2020–2040. https://doi.org/10.1130/B30007.1

Zhang, N., Dang, Z., Huang, C., & Li, Z. X. (2018). The dominant driving force for supercontinent breakup: Plume push or subduction retreat? *Geoscience Frontiers*, *9*(4), 997–1007. https://doi.org/10.1016/j.gsf.2018.01.010

Zhang, N., Zhong, S., & Flowers, R. M. (2012). Predicting and testing continental vertical motion histories since the Paleozoic. *Earth and Planetary Science Letters*, *317-318*, 426–435. https://doi.org/10.1016/j.epsl.2011.10.041

Zhang, N., Zhong, S., Leng, W., & Li, Z. X. (2010). A model for the evolution of the Earth's mantle structure since the Early Paleozoic. *Journal of Geophysical Research - Solid Earth*, *115*(B6). https://doi.org/10.1029/2009JB006896

Zhang, N., Zhong, S., & McNarmara, A. K. (2009). Supercontinent formation from stochastic collision and mantle convection models. *Gondwana Research*, *15*(3-4), 267–275. https://doi.org/10.1016/j.gr.2008.10.002

Zhong, S., & Gurnis, M. (1995). Mantle Convection with Plates and Mobile, Faulted Plate Margins. *Science*, *267*(5199), 838–843. https://doi.org/10.1126/science.267.5199.838

Zhong, S., McNamara, A., Tan, E., Moresi, L., & Gurnis, M. (2008). A benchmark study on mantle convection in a 3-D spherical shell using CitcomS. *Geochemistry, Geophysics, Geosystems*, *9*, Q10017. https://doi.org/10.1029/2008GC002048

Zhong, S., & Watts, A. B. (2013). Lithospheric deformation induced by loading of the Hawaiian Islands and its implications for mantle rheology. *Journal of Geophysical Research: Solid Earth*, *118*, 6025–6048. https://doi.org/10.1002/2013jb010408

Zhong, S., Zhang, N., Li, Z. X., & Roberts, J. H. (2007). Supercontinent cycles, true polar wander, and very long-wavelength mantle convection. *Earth and Planetary Science Letters*, *261*(3–4), 551–564. https://doi.org/10.1016/j.epsl.2007.07.049

Zhong, S., & Zuber, M. T. (2000). Long-wavelength topographic relaxation for self-gravitating planets and implications for the time-dependent compensation of surface topography. *Journal of Geophysical Research, Planets*, *105*(E2), 4153–4164. https://doi.org/10.1029/1999je001075